Published in final edited form as:

Circ Res. 2020 December 04; 127(12): 1536–1548. doi:10.1161/CIRCRESAHA.120.317349.

Ionic Mechanisms of Impulse Propagation Failure in the FHF2-Deficient Heart

David S. Park[1,*], **Akshay Shekhar**[1,4,*], **John Santucci III**[1], **Gabriel Redel-Traub**[1], **Sergio Solinas**[2,3], **Shana Mintz**[1], **Xianming Lin**[1], **Ernest Whanwook Chang**[1], **Deven Narke**[1], **Yuhe Xia**[5], **Mitchell Goldfarb**[3], **Glenn I. Fishman**[1]

[1]The Leon H. Charney Division of Cardiology, New York University School of Medicine, 522 First Avenue, Smilow 801, New York; [2]University of Zurich, Institute of Neuroinformatics, Winterthurerstrasse 190, CH-8057 Zurich, Switzerland; [3]Hunter College of City University, Department of Biological Sciences, Room HN810, 695 Park Avenue, New York; [4]Regeneron Pharmaceuticals 777 Old Saw Mill River Road, Tarrytown, NY 10591, [5]Department of Population Health, New York University School of Medicine, 522 First Avenue, New York.

Abstract

Rationale: Fibroblast growth factor homologous factors (FHFs) are key regulators of sodium channel inactivation. Mutations in these critical proteins have been implicated in human diseases including Brugada syndrome, idiopathic ventricular arrhythmias, and epileptic encephalopathy. The underlying ionic mechanisms by which reduced sodium channel availability in *Fhf2* knockout mice predisposes to abnormal excitability at the tissue level are not well defined.

Objective: Using animal models and theoretical multicellular linear strands, we examined how FHF2 orchestrates the interdependency of sodium, calcium, and gap junctional conductances to safeguard cardiac conduction.

Methods and Results: $Fhf2^{KO}$ mice were challenged by reducing calcium conductance using verapamil or by reducing gap junctional conductance using carbenoxolone or by backcrossing into a connexin 43 heterozygous ($Cx43^{+/-}$) background. All conditions produced conduction block in

Address correspondence to: Dr. Glenn I Fishman, The Leon H. Charney Division of Cardiology, New York University School of Medicine, 522 First Avenue, Smilow 801, New York, glenn.fishman@nyulangone.org, Dr. Mitchell Goldfarb, Hunter College of City University, Department of Biological Sciences, Room HN810, 695 Park Avenue, New York, goldfarb@genectr.hunter.cuny.edu.

AUTHOR CONTRIBUTIONS

D.S.P., A.S., J.S., G.R., S.M., E.W.C., and D.N. designed and performed all in vivo and ex vivo cardiac recordings. X.L. designed and performed all single cell recordings, S.S. and M.G. designed the cardiomyocyte and linear strand computational models and ran all simulations, A.S., J.S., G.R. performed all molecular/cellular biology experiments and genotyping. D.S.P., M.G., and G.I.F. directed the research and co-wrote the paper, with the assistance of J.S. Y.X. performed statistical analysis.

*These authors contributed equally to this work.

DISCLOSURES

The authors declare no conflict of interest.

ONLINE MATERIALS AND METHODS

Supplemental Materials

Expanded Materials & Methods

Online Figures I – VIII

Online Tables I –VIII

References 15–21

Fhf2^{KO} mice, with *Fhf2*^{WT} showing normal impulse propagation. To explore the ionic mechanisms of block in *Fhf2*^{KO} hearts, multicellular linear strand models incorporating FHF2-deficient sodium channel inactivation properties were constructed and faithfully recapitulated conduction abnormalities seen in mutant hearts. The mechanisms of conduction block in mutant strands with reduced calcium conductance or gap junction uncoupling are very different. Enhanced sodium channel inactivation due to FHF2 deficiency shifts dependence onto calcium current to sustain electrotonic driving force, axial current flow, and action potential generation from cell-to-cell. In the setting of gap junction uncoupling, slower charging time from upstream cells conspires with accelerated sodium channel inactivation in mutant strands to prevent sufficient downstream cell charging for action potential propagation.

Conclusions: FHF2-dependent effects on sodium channel inactivation ensure adequate sodium current reserve to safeguard against numerous threats to reliable cardiac impulse propagation.

Graphical Abstract

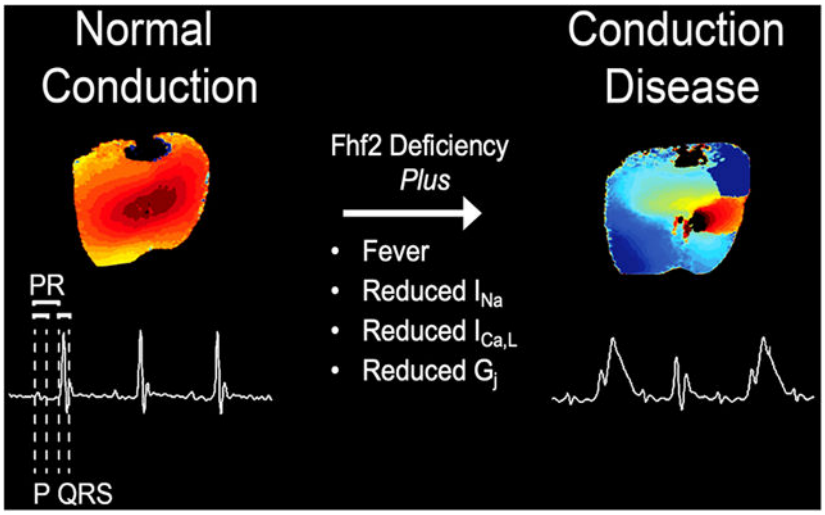

Subject Terms:

Arrhythmias; Electrophysiology; Ion Channels/Membrane Transport; Sudden Cardiac Death; Ventricular Fibrillation

Keywords

Fhf2; *Fgf13*; fibroblast growth factor; impulse propagation; Shaw–Rudy; sodium channel; arrhythmia; Brugada syndrome; conduction; modeling

INTRODUCTION

Cardiac impulse propagation reflects a complex interplay between action potential (AP) generation by excitable cells and passive conduction of the excitation wave front from cell-to-cell. A reduction in either membrane excitability or gap junction coupling can adversely affect impulse propagation by decreasing conduction velocity (CV) or causing conduction block, which increases vulnerability to brady and tachyarrhythmias. Although the

fundamental importance of reliable impulse propagation is indisputable, the factors that influence conduction safety in myocardial tissue have not been rigorously tested. It is well-accepted that the cardiac sodium current (I_{Na}) is the principal determinant of membrane excitability, and therefore conduction, in atrial, Purkinje, and ventricular myocytes. What is less certain, however, is how cardiac conduction is maintained when sodium channel (Na_V) availability is reduced in vivo. A major limitation has been the lack of an animal model with sufficiently low membrane excitability in which the multiplicity of factors that influence impulse propagation can be studied. We[1] and others[2] have recently identified fibroblast growth factor homologous factor 2 (FHF2), also known as fibroblast growth factor 13 (FGF13), as a critical member of the voltage-gated Na_V complex that optimizes cardiac excitability and impulse propagation. In this study, we used the *Fhf2* mouse model to study the limits of conduction behavior and generate FHF2-aware theoretical linear strands to investigate the ionic basis of conduction failure.

FHF2 belongs to a family of FHFs that bind to the cytoplasmic tails of voltage-gated sodium channels and modulates channel gating properties and trafficking[3]. Underscoring their importance as regulators of Na_V function, mutations in FHFs have been implicated in heritable diseases of excitability, including Brugada syndrome[4], atrial and ventricular arrhythmias with sudden cardiac death[5], neonatal onset epileptic encephalopathy[6] and febrile-onset seizures[7]. *Fhf2* knockout mice (*Fhf2*^{KO} mice) exhibit marked conduction abnormalities when challenged with the sodium channel blocking drug flecainide or with temperature elevation. At higher temperatures, *Fhf2*^{KO} mice display a constellation of reversible electrocardiographic (ECG) findings including conduction slowing with eventual conduction block and ECG changes suggestive of Brugada syndrome[1], an arrhythmic condition associated with sodium channel loss-of-function[8–10]. *Fhf2*^{KO} ventricular myocytes have reduced excitability at higher temperature, which is attributable in part to a hyperpolarizing shift of steady-state inactivation of I_{Na} and an accelerated rate of closed-state and open-state Na_V inactivation.

Similar to our findings, Wang and colleagues[2] reported that their cardiac conditional *Fhf2*^{KO} mice have conduction defects that become fully apparent with flecainide treatment. In addition, flecainide triggered ventricular arrhythmias in mutant animals. FHF2-deficient cardiomyocytes exhibit altered action potential characteristics consistent with reduced sodium channel availability, including slower maximal upstroke velocity of phase 0 ($[dV/dt]_{max}$) and reduced action potential amplitude (APA). Defects in the sodium current include a reduction in I_{Na} density by ~25% and hyperpolarization of $V_{1/2}$ of steady state inactivation.

In addition to cardiac conduction defects, FHF2-deficient mice also exhibit temperature sensitive neuronal phenotypes. *Fhf2* heterozygous female mice exhibit hyperthermia-induced seizures likely due to impaired excitability of inhibitory neurons of the hippocampus[7]. Loss of *Fhf2* also causes impaired heat nociception by diminishing $Na_V1.7$ current density resulting in reduced excitability and conduction of dorsal root ganglia neurons[11, 12] (Marra and M. Goldfarb, unpublished data). The collection of cardiac and neuronal phenotypes of *Fhf2*^{KO} mice suggest that FHF proteins may have evolved, in part, to

antagonize temperature-dependent acceleration of Na_V inactivation rates and safeguard excitable tissues such as the heart and brain during transient febrile episodes.

The severe reduction in I_{Na} availability in *Fhf2*^{KO} cardiomyocytes allows us to study the various factors that contribute to conduction behavior *in vivo*. Shaw and Rudy first utilized the theoretical multicellular fiber to study the impact of reduced membrane excitability or gap junction uncoupling on conduction parameters, including CV, $[dV/dt]_{max}$, and safety factor (SF)[13]. SF is a dimensionless parameter calculated as a ratio of charge generated by excitation divided by charge required for depolarization, with SF<1 indicating conduction failure. The Shaw–Rudy model predicts that $I_{Ca,L}$ and gap junctional conductance play a larger role in safe impulse propagation when membrane excitability is reduced. Using the *Fhf2* mouse model, we validate the observations of Shaw and Rudy in a biological context. We also generate FHF2 aware linear strand models that identify distinct mechanisms whereby $I_{Ca,L}$ and G_j contribute to conduction safety.

METHODS

The authors declare that all supporting data are available within the article (and its online supplementary files).

Cardiomyocyte computational model files are available for download at the ModelDB portal (https://senselab.med.yale.edu/modeldb/). All other data and materials, including mouse lines, are available upon corresponding author request.

See Supplemental Material for details on the parameters for the computational model and other experimental procedures.

RESULTS

Fhf2^{KO} mice exhibit increased sensitivity to calcium channel blockade.

To investigate whether $I_{Ca,L}$ contributes to conduction safety in the *Fhf2*^{KO} heart, we challenged *Fhf2*^{WT} and *Fhf2*^{KO} mice with the L-type calcium channel blocker, verapamil (15mg/kg)[22] and measured conduction parameters using surface ECG. *Fhf2*^{KO} mice were highly sensitive to verapamil treatment, developing significant conduction abnormalities on ECG. *Fhf2*^{KO} mice showed uniform lethality due to ventricular asystole with verapamil treatment (Figure 1A,B). Electrocardiographic features included QRS interval prolongation, which is suggestive of conduction block in the His-Purkinje system, and atrioventricular block that ultimately progressed to ventricular asystole (Figure 1B, Online Figure I and Online Table I). In contrast, *Fhf2*^{WT} mice tolerated verapamil treatment without developing QRS interval prolongation or 2nd or 3rd degree atrioventricular block (Figure 1A,B).

As surface ECG is a poor reflection of ventricular myocardial conduction velocity, optical mapping of *Fhf2*^{WT} and *Fhf2*^{KO} hearts using voltage-sensitive dye was performed to examine epicardial impulse propagation and CV at 37°C with and without verapamil treatment (0.25mg/L)[18] (Figure 1C,D and Online Table II). Activation maps of the anterior left ventricular (LV) and right ventricular (RV) walls were obtained at a pacing cycle length of 100ms. *Fhf2*^{WT} hearts displayed normal impulse propagation and normal epicardial CV

irrespective of verapamil treatment. Verapamil did not affect transverse (CV_{min}) or longitudinal (CV_{max}) conduction in *Fhf2*^{WT} hearts (Online Table III). *Fhf2*^{KO} hearts without verapamil displayed reduced conduction velocity, as previously reported[1]. CV was reduced in both transverse and longitudinal axes in *Fhf2*^{KO} hearts, although transverse conduction was disproportionately affected (*Fhf2*^{WT} CV_{min} = 0.42 m/s [0.38, 0.45] versus *Fhf2*^{KO} CV_{min} = 0.14 m/s [0.13, 0.14]; p=0.004 and *Fhf2*^{WT} CV_{max} = 0.76 m/s [0.66, 0.87] versus *Fhf2*^{KO} CV_{max} = 0.42 m/s [0.35, 0.42]; p=0.004; Online Table III). As a result, the anisotropic ratio (CV_{max}/CV_{min}) was significantly increased in *Fhf2*^{KO} hearts (1.78 [1.73, 1.91] in *Fhf2*^{WT} hearts versus 3.29 [3.11, 3.54] in *Fhf2*^{KO} hearts; p=0.004; Online Table III). *Fhf2*^{KO} hearts treated with verapamil developed conduction block during epicardial ventricular pacing. Epicardial CV was not calculated in verapamil treated *Fhf2*^{KO} hearts as conduction block precludes accurate calculation in anisotropically conducting tissues.

We next generated action potential duration (APD) maps of intact *Fhf2*^{WT} and *Fhf2*^{KO} hearts paced at 100ms (Online Figure IIA–C). Unlike a previous report[2] that suggests that APD is prolonged in dissociated ventricular myocytes from cardiac-specific *Fhf2* knockout mice, we show that APD 75 and 90 are not significantly different between *Fhf2*^{WT} and *Fhf2*^{KO} LV and RV. APD50 is significantly shorter in the RV of *Fhf2*^{KO} compared to *Fhf2*^{WT} hearts. (Online Figure IID).

Given a prior report of FHF dependence of voltage-gated calcium current density[23], we empirically measured calcium currents in *Fhf2*^{WT} and *Fhf2*^{KO} ventricular myocytes (Figure 2). Across a broad voltage spectrum, calcium current activation (Figure 2A), steady-state inactivation (Figure 2B), rate of inactivation (Table 1), and peak (Figure 2A; WT pA/pF = 5.38; KO pA/pF = 5.94) were indistinguishable in *Fhf2*^{WT} versus *Fhf2*^{KO} cells. Therefore, the increased dependency of cardiac conduction on $I_{Ca,L}$ in mutant hearts is not due to an FHF2-dependent defect of the calcium current. To rule out the possibility that delayed recovery from inactivation of the fast sodium channel might contribute to conduction block in *Fhf2*^{KO} hearts while pacing at 100ms, whole cell patch clamp recordings performed at −88mV showed recovery from inactivation in *Fhf2*^{KO} cells was more rapid than that of *Fhf2*^{WT} cells (Online Figure III).

Fhf2^{KO} mice display increased sensitivity to reduced gap junctional conductance.

We next explored whether FHF2 deficiency predisposes to conduction block under conditions of gap junction uncoupling. *Fhf2*^{KO} and *Fhf2*^{WT} mice were exposed to the uncoupling agent carbenoxolone (CBX)[24, 25] and conduction parameters were measured by surface ECG. *Fhf2*^{KO} mice developed progressive QRS interval prolongation with CBX treatment in a dose-dependent fashion (Figure 3A,B and Online Table IV). In contrast, *Fhf2*^{WT} mice were resistant to the maximum tested dose of CBX (120mg/kg). Importantly, loss of FHF2 did not affect Cx43 expression levels or localization to intercalated discs (Online Figure IV). We next mated *Fhf2*^{KO} mice into a cardiomyocyte-specific Cx43 heterozygous (Cx43 cHet) background. *Fhf2*^{KO};Cx43 cHet mice displayed prolonged QRS interval duration compared to *Fhf2*^{WT}, Cx43 cHet, and *Fhf2*^{KO} mice, although significance was only present with Cx43 cHet mice (Online Figure V). Sodium current density and voltage dependence of inactivation were indistinguishable between *Fhf2*^{WT} versus Cx43

cHet ventricular myocytes and *Fhf2*^{KO} versus *Fhf2*^{KO};Cx43 cHet ventricular myocytes (Online Figure VI). *Fhf2*^{KO};Cx43 cHet mice were more sensitive to CBX treatment compared to *Fhf2*^{KO} mice (Figure 3A,B). While *Fhf2*^{KO} mice tolerated CBX up to 120mg/kg, the maximum tolerated dose for *Fhf2*^{KO};Cx43 cHet mice was 90mg/kg (Figure 3B and Online Table IV). At CBX 120mg/kg, all *Fhf2*^{KO};Cx43 cHet mice developed marked conduction abnormalities with uniform progression to complete heart block and ventricular asystole.

Optical mapping of *Fhf2*^{WT}, Cx43 cHet, *Fhf2*^{KO}, and *Fhf2*^{KO};Cx43 cHet hearts was performed to evaluate differences in epicardial impulse propagation and CV at 37°C. Activation maps of the anterior LV and RV walls were obtained at a pacing cycle length of 100ms (Figure 3C,D and Online Table V). Consistent with previously published work[1, 20], epicardial CV from Cx43 cHet hearts were not significantly different from *Fhf2*^{WT} controls, whereas *Fhf2*^{KO} hearts had markedly slower CV compared to *Fhf2*^{WT} and Cx43 cHet hearts (0.24 m/sec [0.22, 0.27] vs. 0.54 m/sec [0.53, 0.62], *Fhf2*^{KO} vs *Fhf2*^{WT} LV, respectively $P < 0.05$; 0.24 m/sec [0.22, 0.27] vs. 0.53 m/sec [0.51,0.54], *Fhf2*^{KO} vs Cx43 cHet LV, respectively $P < 0.05$). *Fhf2*^{KO};Cx43 cHet hearts were markedly abnormal and displayed areas of conduction block, precluding epicardial CV measurements.

Computational models of impulse propagation using *Fhf2*^{WT} and *Fhf2*^{KO} cardiomyocytes.

To study the ionic mechanisms of conduction disease in *Fhf2*^{KO} hearts and probe the interdependencies between I_{Na}, $I_{Ca,L}$, and Gj, we generated FHF2-aware computational linear strand models. Our previously described models of *Fhf2*^{WT} and *Fhf2*^{KO} ventricular myocytes incorporated sodium conductance Markov models that gave the same peak amplitude I-NaT at 25°C but with different rate constants for inactivation from closed and open states, consistent with empirical voltage clamp recordings of I-Na_V that showed a 10 mV hyperpolarizing shift in $V_{1/2}$ inactivation in KO cells[1]. Inactivation rates are accelerated with increasing temperature independent of genotype, such that *Fhf2* deletion and elevated temperature combine to give even faster channel inactivation from closed and open states, which is reflected in our cardiomyocyte models. Based on our calcium current recordings, we designed an equivalent voltage-gated calcium conductance for both *Fhf2*^{WT} and *Fhf2*^{KO} ventricular myocyte models (Online Figure VII).

Single-cell cardiomyocyte model cells were assembled into 11-millimeter linear strands by coupling 111 cells end-to-end with a gap junctional conductance (Figure 4A). Gj was set to 772.8 nS at 37°C based prior empirical measurement of Gj between murine ventricular myocytes at room temperature[26] and the temperature Q10 scaling factor of 1.43[27]. Using this value of Gj, our modeled wild-type action potential conduction velocity at 37°C is similar to that determined by voltage optical mapping on epicardially paced ventricular myocardium[1].

Simulation of action potential conduction through *Fhf2*^{WT} and *Fhf2*^{KO} cardiomyocyte model strands at a resting potential of −87 mV was initiated by *in silico* injection of current for 0.5 msec into the first cell of the strand, using sufficient current to drive maximal activation of sodium channels in that cell. For simulations run at 37°C, both *Fhf2*^{WT} and *Fhf2*^{KO} strands faithfully conduct an action potential throughout (Figure 4B,C). The action

potential conducts more slowly and has lower amplitude in the mutant strand in comparison to the wild-type (Online Table VI; *Fhf2*^{KO} CV= 0.339 m/sec, Vpeak = 16.8 mV vs. *Fhf2*^{WT} CV= 0.475 m/sec, Vpeak= 39.7 mV) due to reduced total sodium influx for each cell in the *Fhf2*^{KO} vs. *Fhf2*^{WT} strands (Figure 4D). Reduced sodium current in the *Fhf2*^{KO} strand in comparison to the *Fhf2*^{WT} strand is the combined consequences of greater Na_V steady-state inactivation at the resting potential, further Na_V closed state inactivation during the voltage rise preceding peak Na_V activation, and faster rate of Na_V open state inactivation (Figure 4E,F, Online Table VII). Calcium currents during action potential propagation were similar in both wild-type and mutant strands (Online Figure VIII), reflecting the identical calcium channel formulations in the two strands.

The *Fhf2*^{KO} strand model recapitulates increased sensitivity to sodium channel blockade and temperature elevation demonstrated in knockout mice.

We previously reported that *Fhf2*^{KO} hearts have an increased propensity for conduction block when challenged with the sodium channel blocker flecainide or with hyperthermic stress[1]. Similar to our *in vivo* findings, the *Fhf2*^{KO} strand is far more sensitive to either of these parameter perturbations compared to the *Fhf2*^{WT} strand (Online Table VI). Conduction block in the strand was defined as simulation in which a portion of the strand failed to depolarize or only weakly and passively depolarized without sodium channel activation. To simulate sodium channel blockade, Na_V conductance (gNa_V) was reduced in a graded fashion in *Fhf2*^{WT} and *Fhf2*^{KO} models (Figure 5A,B). The mutant strand undergoes block when gNa_V is reduced by as little as 32%. In contrast, the wild-type strand tolerates a 78% reduction in sodium conductance, which leads to diminished AP amplitude and slowed conduction velocity, but no block is observed. Block occurs at 79% reduction in gNa_V (data not shown). Consistent with reduced sodium channel availability as the mechanism of conduction block in the *Fhf2*^{KO} strand, the maximum upstroke velocity of the action potential ($[dV/dt]_{max}$) is severely reduced at baseline, and similar to the *Fhf2*^{WT} strand, decreases monotonically as gNa_V is reduced (Figure 5C). SF[13] and CV behave similarly to the $[dV/dt]_{max}$ curve when plotted against percentage of gNa_V (Figure 5D,E). The *Fhf2*^{KO} strand also recapitulates the response of mutant hearts to hyperthermic stress, with CV slowing upon temperature elevation[1] prior to conduction block when simulation temperature reaches 41°C, while the *Fhf2*^{WT} strand tolerates temperatures up to and above 45°C with accelerating CV (Figure 5F–H).

The *Fhf2*^{KO} strand model is dependent on calcium current for safe impulse propagation.

We next explored the mechanism underlying verapamil-induced conduction block in *Fhf2*^{KO} hearts. Action potential conduction through the *Fhf2*^{KO} cardiomyocyte strand model is characterized by reduced sodium current flux and a greater percentage of the total inward current carried by calcium ions. Therefore, we suspected that mutant strand models would show enhanced susceptibility to conduction block in response to conditions that reduce calcium conductance. Consistent with this hypothesis, the wild-type strand faithfully conducted without calcium conductance but the *Fhf2*^{KO} strand did not (Figure 6A, B, Online Table VI). The mutant strand underwent progressive decay of the action potential amplitude followed by block if the calcium conductance was reduced to 54% its initial density (Figure 6B). In the absence of FHF2, the contribution of $I_{Ca,L}$ to action potential amplitude is

essential to augment electrotonic driving force between the upstream excited cell and downstream cells. To determine the durability of the $I_{Ca,L}$ contribution to action potential regeneration in the *Fhf2*^{KO} strand, we simulated a condition where gCa_V was set to zero starting from cell 51 and beyond. Under these conditions, the decline of I_{Na} was not seen until cell 52, suggesting that I_{Ca} contributes to forward currents to ensure sufficient Na_V activation in several cells downstream (Figure 6C). The *Fhf2*^{WT} strand displayed virtually normal Na_V activation throughout the fiber despite the abrupt loss of I_{Ca} (Figure 6C).

The *Fhf2*^{KO} strand model demonstrates an increased sensitivity to gap junctional uncoupling.

Based on sodium channel availability at resting potential and more rapid open and closed state Na_V inactivation prior to peak activation, we predicted that *Fhf2*^{KO} models would have a greater sensitivity to junctional uncoupling. Indeed, the *Fhf2*^{KO} strand model recapitulates the enhanced sensitivity to junctional uncoupling seen *in vivo* (Online Table VI). The *Fhf2*^{KO} strand undergoes conduction block at Gj = 5.9 nS, while the *Fhf2*^{WT} strand still conducts at Gj 2.1 nS (Figure 6D,E). The accelerated closed state Na_V inactivation in the mutant strand enhanced its sensitivity to junctional uncoupling. The slow charging process from upstream cells due to junctional uncoupling provided for greater Na_V inactivation and markedly reduced I_{Na} availability (Figure 6F).

We next examined [dV/dt]max and SF when plotted against Gj (Figure 6G,H). The *Fhf2*^{WT} strand displays a rise in $[dV/dt]_{max}$ and SF as Gj is reduced, which reflects preservation of charge in the upstream cell and slower subthreshold depolarization in the downstream cell as coupling between cells decreases. As cells reach near isolated conditions, $[dV/dt]_{max}$ and SF decline as the upstream cell fails to charge the neighboring downstream cell. These relationships also hold true for the mutant strand, although the curves initiate at a lower starting point and fail at significantly higher Gj.

To investigate the role of gCa_V in *Fhf2*^{WT} and *Fhf2*^{KO} strands for conduction safety when Gj is reduced, we plotted $[dV/dt]_{max}$ and SF against Gj with 0% gCa_V in the *Fhf2*^{WT} strand and 70% gCa_V in the *Fhf2*^{KO} strand. In the absence of gCa_V, the profile of $[dV/dt]_{max}$ and SF vs. Gj in the *Fhf2*^{WT} strand is minimally affected (Figure 6G,H), as I_{Na} is the principal component driving upstroke velocity and SF of the action potential. I_{Ca} makes a small contribution to depolarizing current in the *Fhf2*^{WT} strand, such that gCa_V removal slightly left-shifts the Gj point at which junctional uncoupling causes failure. In the *Fhf2*^{KO} strand, I_{Ca} makes a greater contribution to the overall depolarizing current, markedly increasing sensitivity to junctional uncoupling. A 30% reduction in gCa_V left-shifts the Gj point at which junctional uncoupling causes failure of $[dV/dt]_{max}$ and SF by more than 8-fold (Figure 6G,H).

The increased sensitivities of the *Fhf2*^{KO} strand are due to steady state and dynamic reductions to sodium conductance availability.

In order to better understand the individual factors leading to conduction failure in *Fhf2*^{KO} mice, a third model was created, termed: *Fhf2*^{WT}*Na*$_V$^{HYPO}. *Fhf2*^{KO} mice possess reduced Na_V availability as a consequence of a hyperpolarizing shift in Na_V steady state inactivation

and an increased rate of channel inactivation[1]. This third $Fhf2^{WT}Na_V^{HYPO}$ model was designed by reducing the sodium conductance density of the $Fhf2^{WT}$ model to 49% such that the $Fhf2^{WT}Na_V^{HYPO}$ and $Fhf2^{KO}$ models generate the same peak sodium current upon step depolarization from the −87 mV resting potential (Online Table VII). Simulations were run to tease out if the dramatic phenotypes observed in vivo were a consequence of the reduced sodium currents alone, or some additional factor, specifically the gating properties of the channel.

The $Fhf2^{WT}Na_V^{HYPO}$ strand conducts safely at 37°C with AP amplitude and CV less seriously impaired than in the $Fhf2^{KO}$ strand (Online Table VI). In comparison to the $Fhf2^{KO}$ strand, safe conduction through the $Fhf2^{WT}Na_V^{HYPO}$ strand is less sensitive to uncoupling (failure at Gj= 2.9 nS; Online Table VI) or reduction in gNa_V density (failure upon reduction to 42%; Online Table VI). Furthermore, the $Fhf2^{WT}Na_V^{HYPO}$ strand safely conducts when temperature is raised to 45°C or when gCa_V is eliminated (Online Table VI). These findings support the contention that accelerated sodium channel inactivation in the absence of FHF is an important contributor to the multitude of conduction block sensitivities in the $Fhf2^{KO}$ heart.

DISCUSSION

Here we identify FHF2 as an essential component of the cardiac sodium channel complex that ensures I_{Na} availability is sufficient for optimal conduction performance in the murine heart. FHF2-dependent effects on cardiac sodium channel inactivation provide adequate depolarization and kinetic reserve of the sodium current to withstand various threats to safe conduction. We show using both *in vivo* and *in silico* approaches that FHF2 deficiency increases vulnerability to propagation failure when challenged with temperature elevation or reductions in sodium, calcium, or junctional conductance. These results not only validate the findings of the original Shaw–Rudy model but also identify FHFs as the principal modulator of I_{Na} availability that ensures propagation safety.

Although it is unknown precisely when FHFs first appeared in the cardiovascular or nervous systems on an evolutionary timescale, FHFs may have conferred a survival advantage in two ways: 1) to enable I_{Na} dynamics to be modulated rapidly and in a cell-type specific manner to optimize signal processing in neural networks[28, 29] and 2) to ensure sufficient depolarization and kinetic reserve of I_{Na} to protect the heart and nervous system against fever, an essential response to infection. In the heart, $Fhf2^{KO}$ mice develop profound conduction abnormalities, Brugada-like ECG changes, ventricular contractile dyssynchrony[30], and asystole with temperature elevation[1]. In the nervous system, $Fhf2^{KO}$ mice develop hyperthermia-induced seizures attributable to impaired excitability of inhibitory hippocampal neurons[7] as well as defects in heat nociception caused by an inability to sustain action potential firing and conduction in dorsal root ganglia neurons in response to noxious heat stimuli[11, 12] (C.Marra and M. Goldfarb, unpublished data).

The FHF2-aware strand models recapitulate the temperature-dependent propagation failure seen in mutant mice. Conduction defects in the mutant strand is due to a combination of 74% steady-state Na_V inactivation at the resting potential and accelerated closed-state and

open-state Na_V inactivation that markedly reduces I_{Na}. Diminished I_{Na} leaves the mutant strand highly vulnerable to reductions in sodium conductance or to temperature elevation. Temperature elevation causes an enhancement of inactivation rate that synergizes with FHF2 loss-of-function effects on Na_V inactivation to severely suppress I_{Na}.

Our data also demonstrate another critical function of FHF2 in the heart, to decrease the dependency of impulse propagation on $I_{Ca,L}$ or junctional conductance. *Fhf2*^{KO} hearts readily develop conduction block when challenged with either calcium channel blockade or junctional uncoupling. In the absence of FHF2, $I_{Ca,L}$ plays an important role in augmenting depolarization reserve by contributing to action potential amplitude to sustain electronic driving force and axial current flow. The mechanism of conduction block in *Fhf2*^{KO} hearts during junctional uncoupling differs from calcium dependent effects. As the rate of passive charging of downstream cells during the subthreshold depolarization phase in the strand is a function of Gj, uncoupling conspires with more rapid acceleration of Na_V inactivation to markedly diminish sodium channel availability in the mutant strand. We show that conduction fails at a ~3-fold higher level of Gj in the *Fhf2*^{KO} strand compared to the *Fhf2*^{WT} strand. Therefore, FHF2 provides sufficient I_{Na} kinetic reserve by slowing sodium channel closed state inactivation rates, which increases tolerance to transient reductions in gap junctional conductance. By maximizing sodium channel availability, FHF2 ensures that depolarization and kinetic reserve are sufficient so that impulse propagation is dependent on I_{Na} and not $I_{Ca,L}$ and less sensitive to reduced Gj. This configuration also allows for functionally distinct roles between different ionic currents, where I_{Na} is dedicated to conduction and $I_{Ca,L}$ is dedicated to intracellular signaling and myocardial contraction[31].

The full manifestation of conduction defects in *Fhf2*^{KO} mice cannot be explained simply by a reduction in sodium conductance density alone. It is rather the constellation of inactivation defects, including the left shift in steady state inactivation and the accelerated rate of open and closed state inactivation, that yields a myocardial substrate that is highly prone to conduction failure. Whereas the *Fhf2*^{KO} strand developed conduction block when challenged with temperature elevation or reduced gNa_V, gCa_V, or Gj, the *Fhf2*^{WT}*Na*$_V$^{HYPO} strand, which models an equivalent reduction in sodium conductance density to the *Fhf2*^{KO} strand but with wildtype gating parameters, behaves differently when challenged. *Fhf2*^{WT}*Na*$_V$^{HYPO} strand is more resistant to reductions in gNa_V or Gj than the *Fhf2*^{KO} strand and did not block with temperature elevation or elimination of gCa_V. Additionally, conduction failure is not a function of delayed recovery from inactivation or prolonged refractoriness in FHF2 deficient hearts.

The disproportionate effect of FHF2 loss-of-function on transverse CV is an intriguing observation. We have previously shown that sodium current behavior in adult cardiac ventricular myocytes differs as a function of subcellular localization[30]. Peak I_{Na} density was larger when measured at the intercalated disc versus at the lateral membrane. Furthermore, a positive shift in steady-state activation, a negative shift in steady-state inactivation, and a slower recovery from inactivation were observed in I_{Na} at the lateral membrane. Based on these observations, the majority of sodium channels in the lateral membrane of ventricular myocytes would be predicted to be inactivated at resting potential. Consequently, transverse conduction may be especially vulnerable to the added insult of FHF2 deficiency.

Measurements of subcellular sodium current behavior in *FHF2*^{KO} ventricular myocytes and incorporation of these data into two dimensional models will be required to test this hypothesis. Moreover, such an approach may provide additional insight into the mechanisms of arrhythmogenesis in the Fhf2 knockout mice, which develop spontaneous ventricular arrhythmias when challenged with flecainide[2].

Our study identifies FHF2 as the major component of the cardiac sodium channel macromolecular complex that ensures adequate depolarization and kinetic reserve of I_{Na} for optimal conduction performance in the murine heart. Remarkably, we show that FHF2 is singularly sufficient to protect against conduction block due to hyperthermic stress and in response to reductions in $I_{Ca,L}$ or Gj. It will be of interest to determine how cardiovascular diseases, such as myocardial ischemia or heart failure, influence FHF expression levels or interactions with other components of the cardiac sodium channel complex. Furthermore, given that FHF2 is an X-linked gene, examination of sex-based differences is in order, and will be the focus of ongoing work. Another important question is whether FHF1, the dominant family member expressed in human ventricular myocytes, behaves in a similar manner to FHF2. This has become all the more important as FHF1 (aka FGF12) was reported to be a candidate Brugada syndrome locus[4]. A missense mutation in FGF12 (Q7R-FGF12) decreased binding to the $Na_V1.5$ C terminus, reducing sodium current density and sodium channel availability. Incorporation of these FHF1-dependent changes on the sodium current into our theoretical multicellular fiber will be an important tool for unraveling disease pathogenesis in these and related patients, and may also be of use in formulating mutation and mechanism-specific therapies. Lastly, our results underscore the importance of Na_V inactivation properties in maintaining normal cardiac excitation and conduction and suggest that targeting inactivation may prove a fruitful strategy for enhancing depolarization and kinetic reserve to preserve safe conduction.

Supplementary Material

Refer to Web version on PubMed Central for supplementary material.

ACKNOWLEDGEMENTS

We thank Fang-Yu Liu and Jie Zhang for their technical assistance.

SOURCES OF FUNDING

Supported by National Institutes of Health grants (R01HL142498 to G.I.F. and T32 GM066704 and F31 HL132438 to A.S.) and a Fondation Leducq Transatlantic Network of Excellence Award (G.I.F. and D.S.P.)

Nonstandard Abbreviations and Acronyms:

FHF2	fibroblast growth factor homologous factor 2
FGF13	fibroblast growth factor 13
CV	conduction velocity
I_{Na}	sodium current

$\mathbf{I_{Ca,\,L}}$	L-type calcium current
Gj	junctional conductance
$\mathbf{[dV/dt]_{max}}$	maximum upstroke velocity of the action potential
SF	safety factor

REFERENCES

1. Park DS, Shekhar A, Marra C, Lin X, Vasquez C, Solinas S, Kelley K, Morley G, Goldfarb M and Fishman GI. Fhf2 gene deletion causes temperature-sensitive cardiac conduction failure. Nat Commun. 2016;7:12966. [PubMed: 27701382]
2. Wang X, Tang H, Wei EQ, Wang Z, Yang J, Yang R, Wang S, Zhang Y, Pitt GS, Zhang H and Wang C. Conditional knockout of Fgf13 in murine hearts increases arrhythmia susceptibility and reveals novel ion channel modulatory roles. J Mol Cell Cardiol. 2017;104:63–74. [PubMed: 28119060]
3. Goldfarb M Voltage-gated sodium channel-associated proteins and alternative mechanisms of inactivation and block. Cell Mol Life Sci. 2012;69:1067–76. [PubMed: 21947499]
4. Hennessey JA, Marcou CA, Wang C, Wei EQ, Wang C, Tester DJ, Torchio M, Dagradi F, Crotti L, Schwartz PJ, Ackerman MJ and Pitt GS. FGF12 is a candidate Brugada syndrome locus. Heart Rhythm. 2013;10:1886–94. [PubMed: 24096171]
5. Musa H, Kline CF, Sturm AC, Murphy N, Adelman S, Wang C, Yan H, Johnson BL, Csepe TA, Kilic A, Higgins RS, Janssen PM, Fedorov VV, Weiss R, Salazar C, Hund TJ, Pitt GS and Mohler PJ. SCN5A variant that blocks fibroblast growth factor homologous factor regulation causes human arrhythmia. Proc Natl Acad Sci U S A. 2015;112:12528–33. [PubMed: 26392562]
6. Siekierska A, Isrie M, Liu Y, Scheldeman C, Vanthillo N, Lagae L, de Witte PA, Van Esch H, Goldfarb M and Buyse GM. Gain-of-function FHF1 mutation causes early-onset epileptic encephalopathy with cerebellar atrophy. Neurology. 2016;86:2162–70. [PubMed: 27164707]
7. Puranam RS, He XP, Yao L, Le T, Jang W, Rehder CW, Lewis DV and McNamara JO. Disruption of Fgf13 causes synaptic excitatory-inhibitory imbalance and genetic epilepsy and febrile seizures plus. J Neurosci. 2015;35:8866–81. [PubMed: 26063919]
8. Brugada J, Brugada P and Brugada R. The syndrome of right bundle branch block ST segment elevation in V1 to V3 and sudden death--the Brugada syndrome. Europace. 1999;1:156–66. [PubMed: 11225790]
9. Brugada P and Brugada J. Right bundle branch block, persistent ST segment elevation and sudden cardiac death: a distinct clinical and electrocardiographic syndrome. A multicenter report. J Am Coll Cardiol. 1992;20:1391–6. [PubMed: 1309182]
10. Chen Q, Kirsch GE, Zhang D, Brugada R, Brugada J, Brugada P, Potenza D, Moya A, Borggrefe M, Breithardt G, Ortiz-Lopez R, Wang Z, Antzelevitch C, O'Brien RE, Schulze-Bahr E, Keating MT, Towbin JA and Wang Q. Genetic basis and molecular mechanism for idiopathic ventricular fibrillation. Nature. 1998;392:293–6. [PubMed: 9521325]
11. Yang L, Dong F, Yang Q, Yang PF, Wu R, Wu QF, Wu D, Li CL, Zhong YQ, Lu YJ, Cheng X, Xu FQ, Chen L, Bao L and Zhang X. FGF13 Selectively Regulates Heat Nociception by Interacting with Nav1.7. Neuron. 2017;93:806–821 e9. [PubMed: 28162808]
12. Effraim PR, Huang J, Lampert A, Stamboulian S, Zhao P, Black JA, Dib-Hajj SD and Waxman SG. Fibroblast growth factor homologous factor 2 (FGF-13) associates with Nav1.7 in DRG neurons and alters its current properties in an isoform-dependent manner. Neurobiol Pain. 2019;6:100029. [PubMed: 31223136]
13. Shaw RM and Rudy Y. Ionic mechanisms of propagation in cardiac tissue. Roles of the sodium and L-type calcium currents during reduced excitability and decreased gap junction coupling. Circ Res. 1997;81:727–41. [PubMed: 9351447]
14. Hines ML and Carnevale NT. NEURON: a tool for neuroscientists. Neuroscientist. 2001;7:123–35. [PubMed: 11496923]

15. Bondarenko VE, Szigeti GP, Bett GC, Kim SJ and Rasmusson RL. Computer model of action potential of mouse ventricular myocytes. Am J Physiol Heart Circ Physiol. 2004;287:H1378–403. [PubMed: 15142845]
16. Cohen SD, Hindmarsh AC and Dubois PF. CVODE, a stiff/nonstiff ODE solver in C Computers in Physics. 1996;10:138–143.
17. Gutstein DE, Morley GE, Tamaddon H, Vaidya D, Schneider MD, Chen J, Chien KR, Stuhlmann H and Fishman GI. Conduction slowing and sudden arrhythmic death in mice with cardiac-restricted inactivation of connexin43. Circ Res. 2001;88:333–9. [PubMed: 11179202]
18. Aydin O, Becker R, Kraft P, Voss F, Koch M, Kelemen K, Katus HA and Bauer A. Effects of protein kinase C activation on cardiac repolarization and arrhythmogenesis in Langendorff-perfused rabbit hearts. Europace. 2007;9:1094–8. [PubMed: 17684067]
19. Gloschat C, Aras K, Gupta S, Faye NR, Zhang H, Syunyaev RA, Pryamonosov RA, Rogers J, Kay MW and Efimov IR. RHYTHM: An Open Source Imaging Toolkit for Cardiac Panoramic Optical Mapping. Sci Rep. 2018;8:2921. [PubMed: 29440763]
20. Morley GE, Vaidya D, Samie FH, Lo C, Delmar M and Jalife J. Characterization of conduction in the ventricles of normal and heterozygous Cx43 knockout mice using optical mapping. J Cardiovasc Electrophysiol. 1999;10:1361–75. [PubMed: 10515561]
21. Lang D, Glukhov AV, Efimova T and Efimov IR. Role of Pyk2 in cardiac arrhythmogenesis. Am J Physiol Heart Circ Physiol. 2011;301:H975–83. [PubMed: 21666110]
22. Choi JS and Li X. The effect of verapamil on the pharmacokinetics of paclitaxel in rats. Eur J Pharm Sci. 2005;24:95–100. [PubMed: 15626582]
23. Hennessey JA, Wei EQ and Pitt GS. Fibroblast growth factor homologous factors modulate cardiac calcium channels. Circ Res. 2013;113:381–8. [PubMed: 23804213]
24. Hosseinzadeh H and Nassiri Asl M. Anticonvulsant, sedative and muscle relaxant effects of carbenoxolone in mice. BMC Pharmacol. 2003;3:3. [PubMed: 12720572]
25. Hashizume M, Miyazaki T, Sakimura K, Watanabe M, Kitamura K and Kano M. Disruption of cerebellar microzonal organization in GluD2 (GluRdelta2) knockout mouse. Front Neural Circuits. 2013;7:130. [PubMed: 23970854]
26. Yao JA, Gutstein DE, Liu F, Fishman GI and Wit AL. Cell coupling between ventricular myocyte pairs from connexin43-deficient murine hearts. Circ Res. 2003;93:736–43. [PubMed: 14500334]
27. Bukauskas FF and Weingart R. Temperature dependence of gap junction properties in neonatal rat heart cells. Pflugers Arch. 1993;423:133–9. [PubMed: 7683787]
28. Smallwood PM, Munoz-Sanjuan I, Tong P, Macke JP, Hendry SH, Gilbert DJ, Copeland NG, Jenkins NA and Nathans J. Fibroblast growth factor (FGF) homologous factors: new members of the FGF family implicated in nervous system development. Proc Natl Acad Sci U S A. 1996;93:9850–7. [PubMed: 8790420]
29. Dover K, Marra C, Solinas S, Popovic M, Subramaniyam S, Zecevic D, D'Angelo E and Goldfarb M. FHF-independent conduction of action potentials along the leak-resistant cerebellar granule cell axon. Nat Commun. 2016;7:12895. [PubMed: 27666389]
30. Shekhar A, Aristizabal O, Fishman GI, Phoon CKL and Ketterling JA. Characterization of vortex flow in a mouse model of ventricular dyssynchrony by plane-wave ultrasound using hexplex processing. IEEE Trans Ultrason Ferroelectr Freq Control. 2020;PP.
31. Liebeskind BJ, Hillis DM and Zakon HH. Evolution of sodium channels predates the origin of nervous systems in animals. Proc Natl Acad Sci U S A. 2011;108:9154–9. [PubMed: 21576472]

NOVELTY AND SIGNIFICANCE

What Is Known?

- Cardiac sodium channels are the principal determinant of conduction behavior in the heart.
- Fibroblast growth factor homologous factors (FHFs) are important modulators of sodium channels that have been implicated in heart rhythm and seizure disorders.
- *Fhf2* knockout (*Fhf2*^{KO}) mice exhibit defects in sodium channel inactivation that give rise to severe conduction defects in the heart.

What New Information Does This Article Contribute?

- Changes in sodium channel inactivation due to Fhf2 deficiency increases the dependency of cardiac conduction onto auxiliary factors, including calcium and gap junctional conductances.
- FHF2 aware computational models faithfully recapitulate conduction abnormalities seen in mutant hearts and elucidate distinct mechanisms by which sodium, calcium, and gap junctional conductances contribute to conduction in the absence of FHF2.

FHFs are key regulators of sodium channel (Na_V) behavior. Na_V and FHF mutations have been implicated in human heart rhythm (ie. Brugada syndrome) and seizure (ie. epileptic encephalopathy) disorders. *Fhf2*^{KO} mice exhibit cardiac conduction disease and arrhythmias when challenged with temperature elevation and sodium channel blockade. Studies at the cellular level have identified that FHF2 modulates Na_V inactivation properties to optimize channel availability and membrane excitability. What remains unresolved is how altered Na_V gating in *Fhf2*^{KO} hearts influences conduction properties at the tissue level. Here we show that *FHF2*^{KO} hearts are vulnerable to conduction block when challenged with a broad range of stressors, including reduced calcium or gap junctional conductance. Using FHF2 aware theoretical linear strands, we define the underlying ionic mechanisms of conduction failure, which differs depending on the pathological insult. Our findings underscore the importance of Na_V inactivation properties in maintaining normal cardiac excitation and conduction and suggest that targeting FHF2-dependent Na_V inactivation may prove a fruitful strategy for preserving safe conduction in the heart.

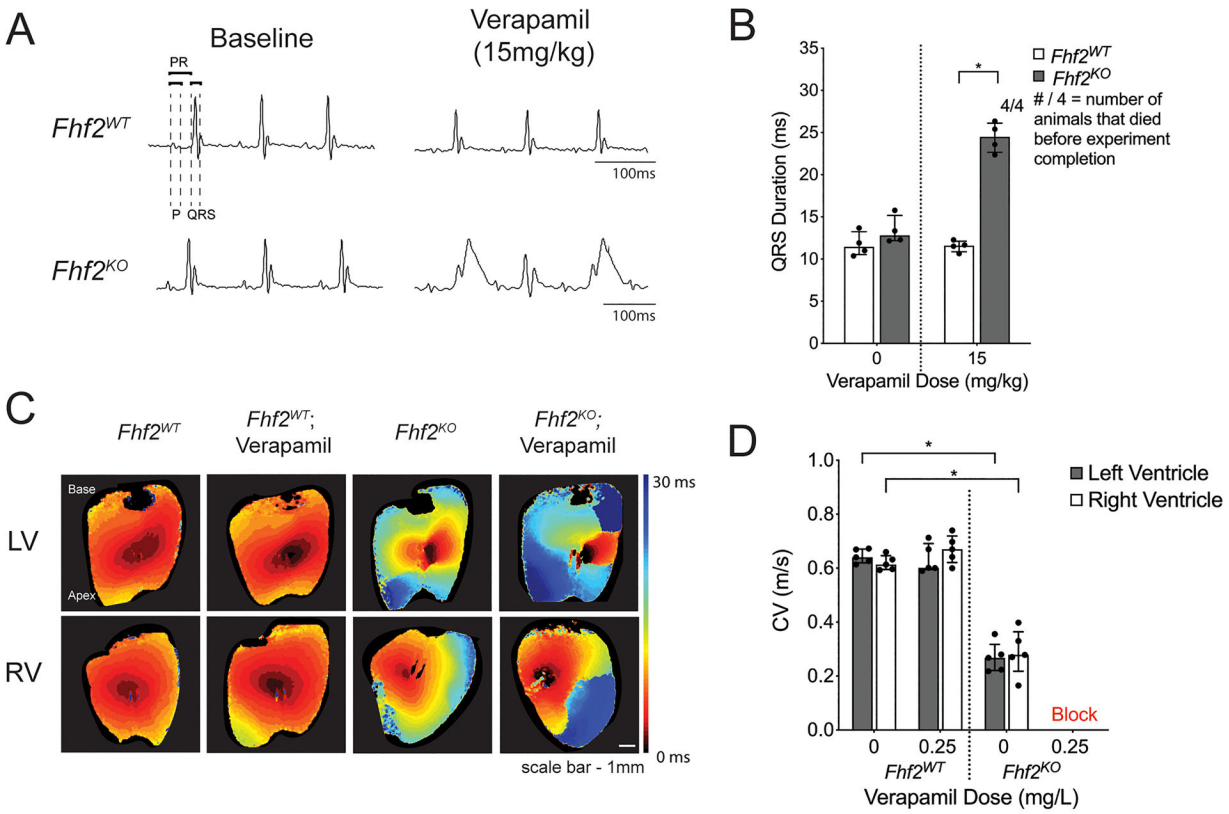

Figure 1. Pharmacological L-type calcium channel blockade produces conduction defects in *Fhf2*^{KO} hearts.

(A,B) *In vivo* experiments with calcium channel blocker verapamil. (A) Representative surface ECG tracings of *Fhf2*^{WT} (n=4) and *Fhf2*^{KO} (n=4) mice subjected to verapamil (0mg/kg or 15mg/kg) via intraperitoneal (IP) injection and observed over 30 minutes. (B) QRS duration plotted against verapamil dose at 0mg/kg or 15mg/kg. QRS measured at 30 minutes or at last measurable time point prior to the onset of complete atrioventricular block. *Fhf2*^{WT} treated with verapamil displayed no changes in QRS duration, and all mice survived verapamil treatment. *Fhf2*^{KO} treated with verapamil experienced QRS prolongation and complete atrioventricular block. None of the *Fhf2*^{KO} mice survived verapamil treatment. (C) Representative epicardial left and right ventricular activation maps. Multiple regions of conduction block were observed in *Fhf2*^{KO} hearts (n=5) after treatment with verapamil. *Fhf2*^{WT} hearts (n=5) did not show any change in CV after treatment. Hearts were paced at 100 milliseconds basic cycle length. Isochronal maps were generated based on the time to action potential peak. Isochrones are drawn 5 milliseconds apart. Time-scale index shown in sidebar. (D) Quantification of left and right ventricular epicardial conduction velocity before and after treatment with verapamil. Multiple regions of block precluded quantitative epicardial CV measurements in *Fhf2*^{KO} hearts treated with verapamil. Data represent median ± interquartile range. *significant p values < 0.05, Wilcoxon signed-rank test was performed for comparisons between paired samples; Mann–Whitney U-test used for comparison of independent variables. See Online Table VIII for individual p-values.

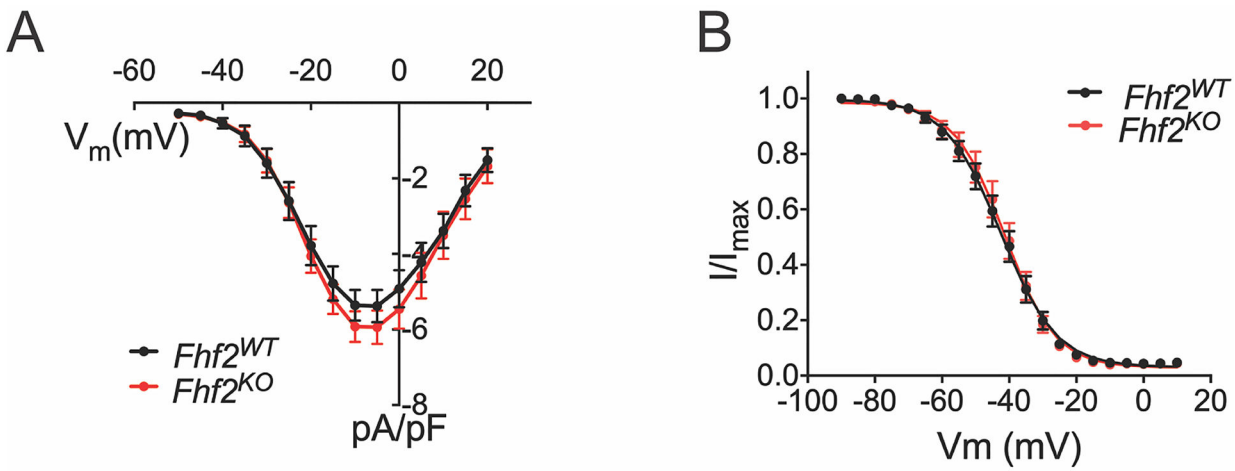

Figure 2. Measured calcium currents are similar in *Fhf2*^{WT} and *Fhf2*^{KO} cardiomyocytes.

(A) Calcium current density as a function of voltage. 200 ms voltage pulses were applied from holding Vm −90 mV to between −50 mV and +30mV in 5mV steps. *Fhf2*^{WT} and *Fhf2*^{KO} cardiomyocytes do not differ in peak calcium current density or voltage dependence of channel activation. (B) Cardiomyocyte voltage-gated calcium channel steady-state inactivation. Available I_{Ca} at 25°C after 500 ms conditioning at voltages spanning −130 to −20 mV is expressed as fraction of maximal I_{Ca}. Voltage dependence of inactivation does not significantly differ between *Fhf2*^{WT} and *Fhf2*^{KO} cardiomyocytes. (n=3 mice in each cohort, 10 cells/mouse). Data presented as mean ± standard error of the mean. Two-sample Kolmogorov-Smirnov test was used to compare current behavior between genotypes. Online Table VIII for individual p-values.

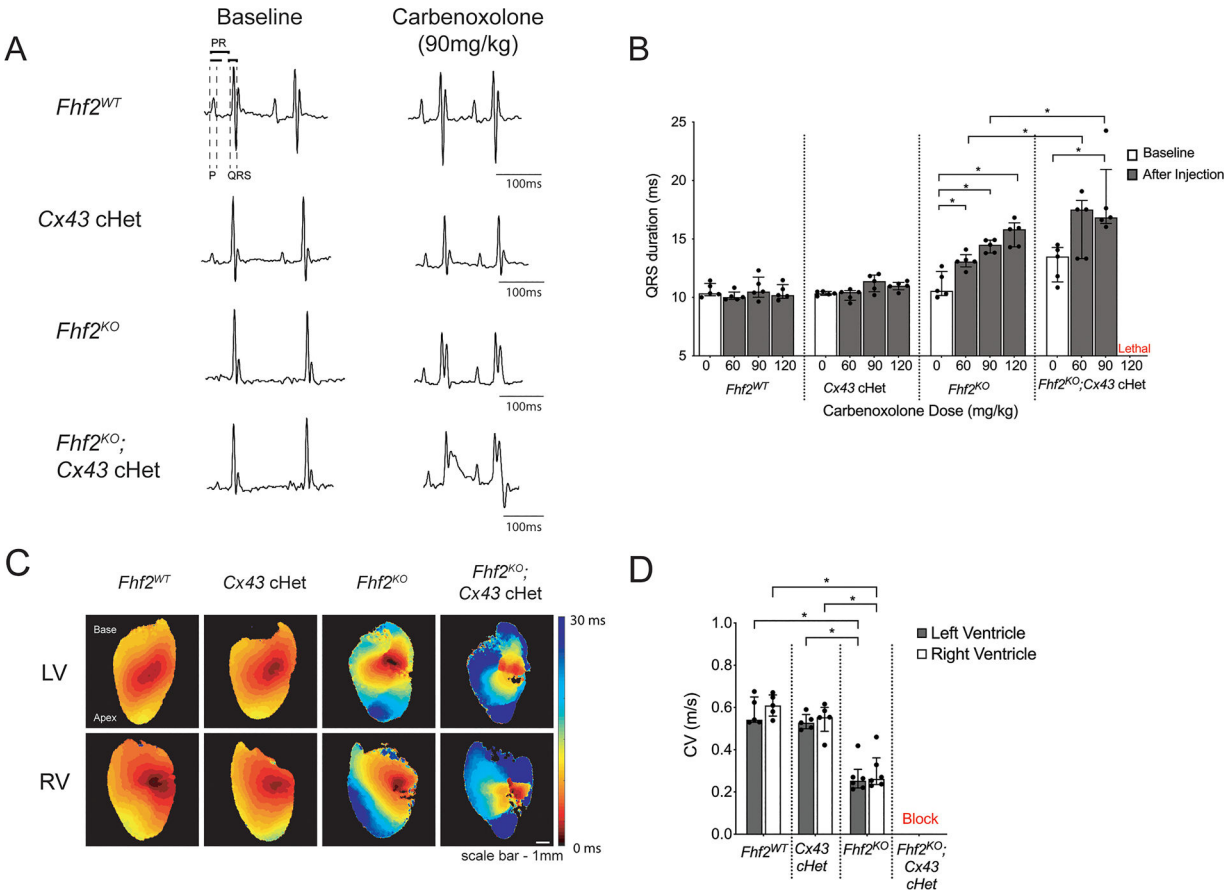

Figure 3. *Fhf2*^{KO} hearts have increased sensitivity to reduced gap junctional conductance.

(A,B) *In vivo* experiments with reduced gap junctional conductance using carbenoxolone or by mating into a cardiomyocyte-specific Cx43 heterozygous (Cx43 cHet) background. (A) Representative surface ECG tracings of *Fhf2*^{WT}, Cx43 cHet, *Fhf2*^{KO}, and *Fhf2*^{KO};Cx43 cHet mice subjected to carbenoxolone. (B) QRS duration plotted against varying doses of carbenoxolone (60mg/kg, 90mg/kg, and 120mg/kg) via intraperitoneal (IP) injection and observed over 30 minutes (n=5 mice per cohort). (C) Representative epicardial left and right ventricular activation maps. Multiple regions of conduction block were observed in *Fhf2*^{KO}; *Cx43* cHet hearts during epicardial pacing. Hearts were paced at 100 milliseconds basic cycle length. Isochrones are drawn 5 milliseconds apart (n=5 mice per cohort). (D) Quantification of left and right ventricular epicardial conduction velocity. Multiple regions of block precluded quantitative epicardial CV measurements in *Fhf2*^{KO}*; Cx43* cHet hearts. Data represent median ± interquartile range. *significant p values < 0.05, Wilcoxon signed-rank test was performed for comparisons between paired samples; Mann–Whitney U-test used for comparison of independent variables; Kruskal-Wallis test for more than two groups followed by Benjamin-Hochberg post-hoc test for pairwise comparisons. See Online Table VIII for individual p-values.

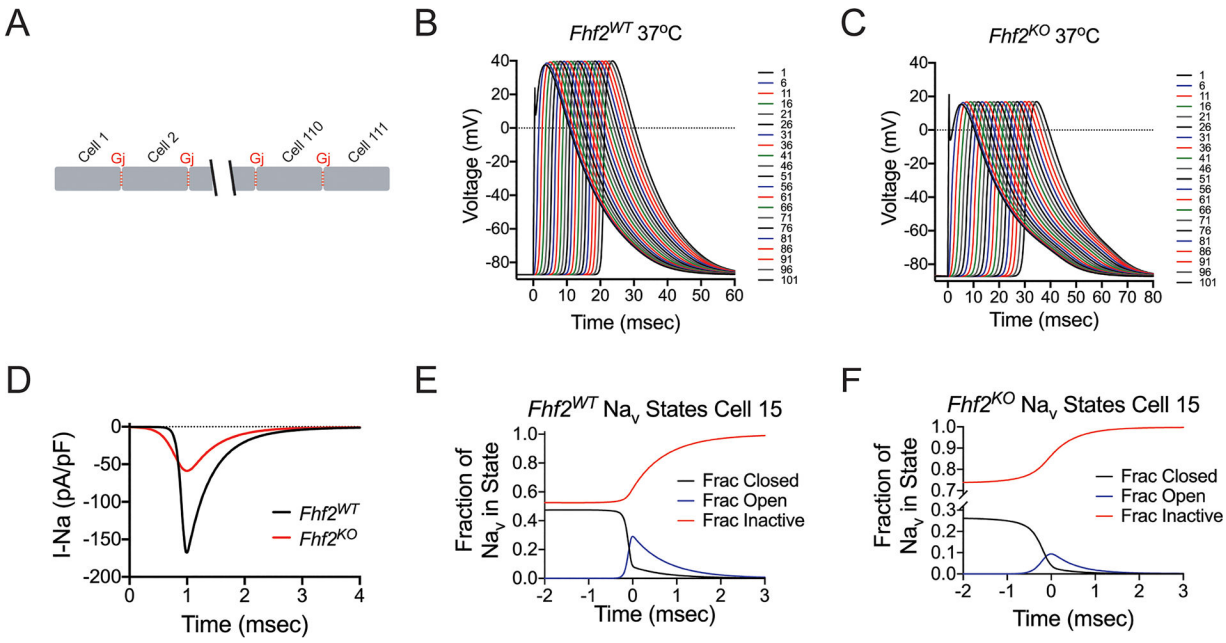

Figure 4. Computational models of *Fhf2*^{WT} and *Fhf2*^{KO} cardiomyocyte strands.

(A) Strand model designed to include 111 cells, each measuring 100 microns aligned end-to-end, connected by gap junctions (Gj = 772.8 nS at 37°C). (B) Simulation of action potential (AP) propagation through strand. 0.5msec current injection into the first cell results in AP propagation through entire *Fhf2*^{WT} strand. The AP propagates with conduction velocity (CV) = 0.475 mm/msec. (C) Similar injection of current into the *Fhf2*^{KO} strand results in slowed AP propagation (CV = 0.339 mm/msec) with decreased AP amplitude in all cells. (D) Sodium current influx in cell 50 as a function of time. Sodium current influx is reduced in the *Fhf2*^{KO} strand, despite the same density of sodium conductance (gNa_V). (E) In cell 15 of the *Fhf2*^{WT} strand, sodium channel availability is approximately 50% at resting potential with peak Na_V activation peaking much earlier than Na_V inactivation. (F) In cell 15 of the *Fhf2*^{KO} strand, reduced sodium current is the consequence of approximately 74% Na_V steady-state inactivation at the resting potential, further Na_V closed state inactivation during the voltage rise preceding peak Na_V activation, and faster decay of the current due to faster Na_V open state inactivation.

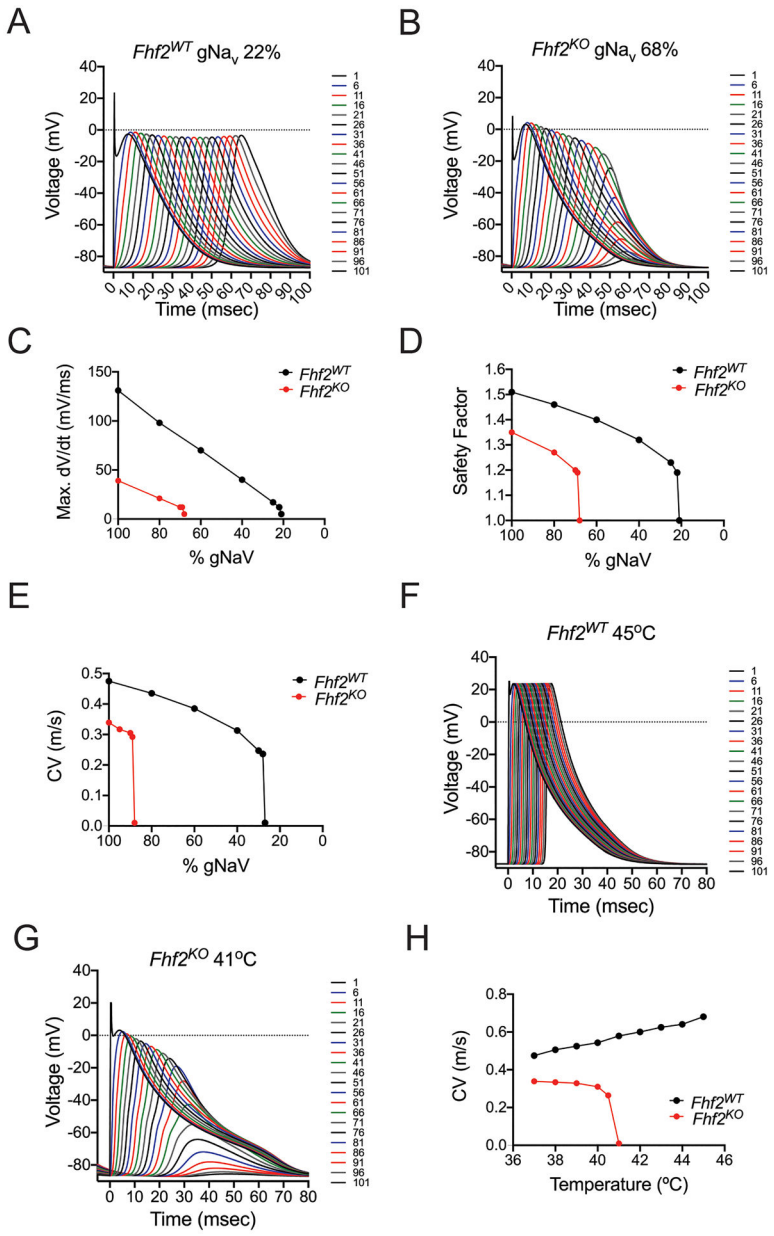

Figure 5. *Fhf2*^{KO} strands are susceptible to conduction failure with reduction in gNa_V and elevated temperatures.

(A) In *Fhf2*^{WT} strand, a 78% reduction in sodium conductance leads to diminished action potential (AP) amplitude and slowed conduction velocity, but no block is observed. (B) In *Fhf2*^{KO} strand, a 32% reduction in sodium conductance leads to progressive decay in AP amplitude, and conduction block. (C) [dV/dt]max for *Fhf2*^{WT} and *Fhf2*^{KO} strands plotted versus reductions in gNa_V. For each strand, [dV/dt]max declines as gNa_V decreases until point of failure. (D) Safety factor for *Fhf2*^{WT} and *Fhf2*^{KO} strands plotted versus reductions in gNa_V. SF declines as gNa_V decreases until point of failure. (E) Conduction velocity for *Fhf2*^{WT} and *Fhf2*^{KO} strands plotted versus reductions in gNa_V. For each strand, CV declines as gNa_V decreases until point of failure. (F) The *Fhf2*^{WT} strand faithfully conducts action potentials when temperature is increased to 45°C. (G) The *Fhf2*^{KO} strand fails to conduct at

41°C due to faster rates of open and closed state inactivation. (H) Conduction velocity for $Fhf2^{WT}$ and $Fhf2^{KO}$ strands plotted versus rising temperature. CV increases with temperature in the $Fhf2^{WT}$ strand, while decreasing in the $Fhf2^{KO}$ strand until failure temperature.

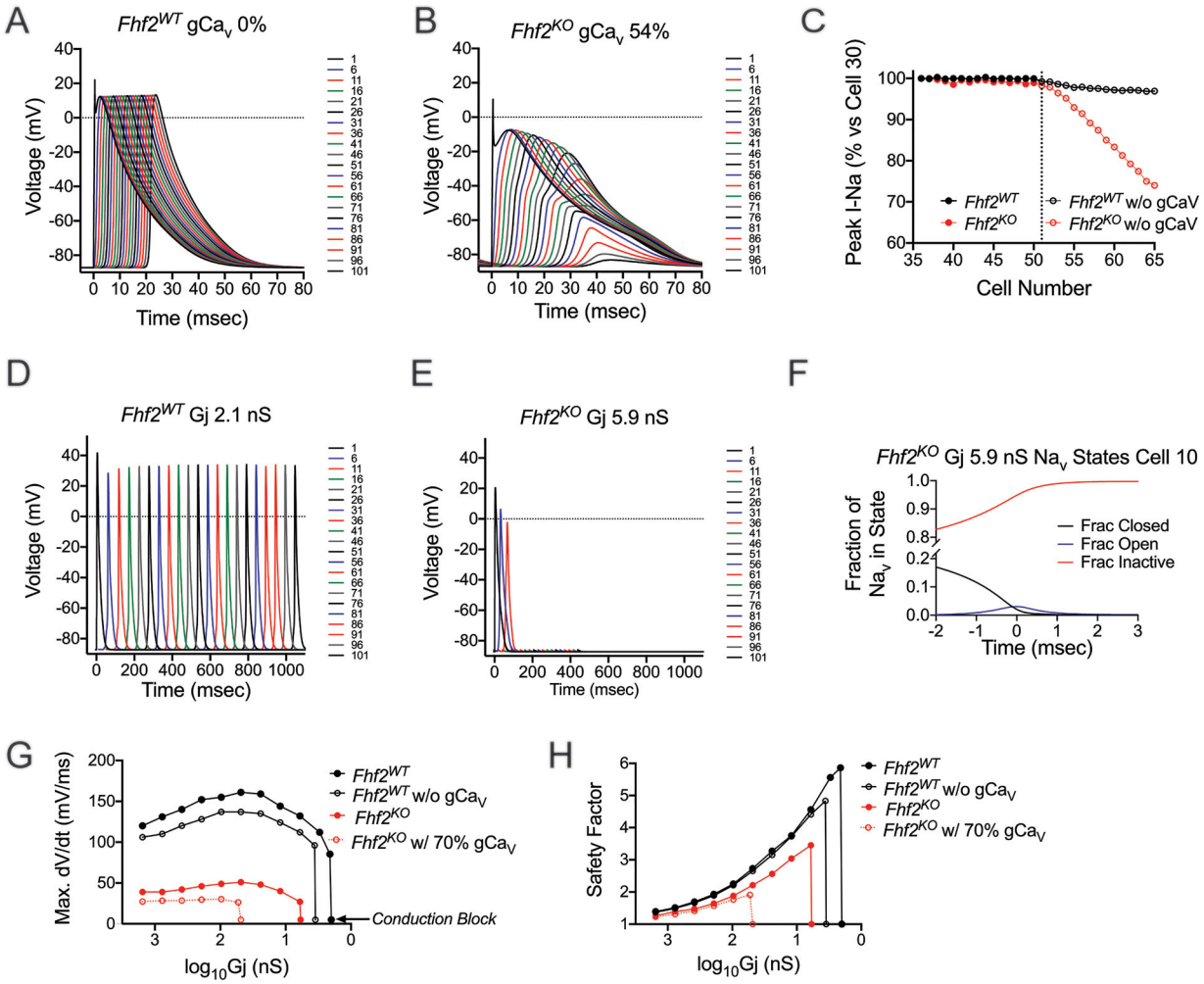

Figure 6. *Fhf2*^{KO} computational strand has increased dependence on calcium currents and gap junctional conductance.

(A) *Fhf2*^{WT} strand model shows no dependence on calcium currents for the propagation of the AP. (B) Reduction of calcium currents to 54% leads to progressive decay of the AP and block in *Fhf2*^{KO} strand. Simulated data are consistent with *in vivo* administration of verapamil. (C) In the *Fhf2*^{KO} strand, when calcium current is set to zero at and beyond cell 51, not until cell 52 is a decrease in peak sodium current noted, with a steady decline thereafter until impulse propagation failure. In contrast, the *Fhf2*^{WT} strand is virtually unaffected by reductions in calcium currents. (D) In the *Fhf2*^{WT} strand, reduction in gap junctional conduction to 2.1 nS dramatically slows conduction, but does not lead to block. Block occurs at Gj of 2.0 nS (data not shown). (E) Reduction of Gj to 5.9 nS in the *Fhf2*^{KO} strand leads to block. (F) In the *Fhf2*^{KO} strand with reduced junctional conductance as in panel E, poor charging from upstream cells results in greater Na_V channel inactivation and diminished I_{Na}. (G,H) *Fhf2*^{KO} strand demonstrates increased reliance of $I_{Ca,L}$ and G_j for safe conduction. (G) A biphasic relationship exists between maximum upstroke velocity ($[dV/dt]_{max}$) and junctional currents in both *Fhf2*^{KO} and *Fhf2*^{WT} strands, with *Fhf2*^{KO} strand showing markedly reduced maximum upstroke velocity and increased dependence on Gj at baseline conditions. Elimination of calcium currents in *Fhf2*^{WT} model only slightly reduces

$[dV/dt]_{max}$ at all Gj values and has virtually no impact on the threshold value of Gj causing block. By contrast, reduction of calcium conductance in the *Fhf2*^{KO} model causes a far greater left shift in the threshold value of Gj inducing block. (H) Safety factor rises as junctional conductance decreases until nearing uncoupling values that cause conduction block. Reduction in calcium currents has only minimal effect on SF in both *Fhf2*^{WT} and *Fhf2*^{KO} strands at Gj values sufficient for safe conduction, while more dramatically impacting the Gj for conduction block in the *Fhf2*^{KO} strand.

Table 1:

Calcium channel inactivation rates.

The rate of I_{Ca} decline at −20mV, −10mV, or 0mV was fitted to a two-component exponential decay. The fast and slow time constants and the fraction of current associated with each decay component do not significantly differ between *Fhf2*^{WT} and *Fhf2*^{KO} cardiomyocytes at any tested voltage. (n=2 mice in each cohort, N=8 *Fhf2*^{WT} cells, N=9 *Fhf2*^{KO} cells). Data presented as mean ± standard error of the mean. Mann–Whitney U-test used for comparison of independent variables. See Online Table VIII for individual p-values.

	WT (N=8)	KO (N=9)	WT (N=8)	KO (N=9)	WT (N=8)	KO (N=9)	WT (N=8)	KO (N=9)
Voltage (mV)	**Tau1 Fraction**	**Tau1 Fraction**	**Tau1 (ms)**	**Tau1 (ms)**	**Tau2 Fraction**	**Tau2 Fraction**	**Tau2 (ms)**	**Tau2 (ms)**
−20	0.53 +/− 0.04	0.49 +/− 0.03	111 +/− 12	114 +/− 12	0.48 +/− 0.04	0.53 +/− 0.04	19.2 +/− 1.7	15.8 +/− 2.1
−10	0.50 +/− 0.05	0.44 +/− 0.05	77 +/− 5	73 +/− 4	0.50 +/− 0.05	0.56 +/− 0.06	17.9 +/− 1.9	14.7 +/− 1.5
0	0.52 +/− 0.06	0.45 +/− 0.05	73 +/− 5	72 +/− 6	0.48 +/− 0.06	0.55 +/− 0.05	20.5 +/− 1.9	17.7 +/− 1.8

Animals (in vivo studies)

Species	Vendor or Source	Background Strain	Sex	Persistent ID / URL
Fhf2^{KO} mice	In house generated	129/svPas	Male/Female	MGI:4434341; Park et al., Nat Com 2016
Cx43$^{flox/+}$; mice (*Gja1*^{tm1Gfi})	In house generated	C57Bl/6J	Male/Female	MGI:3051881; Gutstein et al., Circ Res 2001
α-MHC-Cre mice (Tg(Myh6-cre)2182Mds)	Jackson Labs	FVB/N	Male/Female	MGI:2386742; Agah et al., JCI 1997; https://www.jax.org/strain/011038
Fhf2^{KO}; *Cx43*$^{flox/+}$; α-MHC-Cre mice	In house generated	Backcrossed more than four generations on the 129/svPas background	Male/Female	This study

Antibodies

Target antigen (antimouse if not indicated otherwise)	Host Species	Vendor or Source Catalog #	Working concentration	Persistent ID / URL
Primary Antibodies:				
CX43	Rabbit	Sigma Aldrich C6219	1:100	https://www.sigmaaldrich.com/catalog/nroduct/sigma/c6219
N-Cadherin	Mouse	BD Biosciences, 610921	1:100	https://www.bdbiosciences.com/us/annlications/research/stem-cell-research/cancer-research/human/nurified-mouse-anti-n-cadherin-32n-cadherin/n/610921
Secondary Antibodies:				
Donkey anti-Rabbit, Alexa Fluor 594	Donkey	Invitrogen, A32754	1:400	https://www.thermofisher.com/antibody/nroduct/Donkey-anti-Rabbit-IgG-H-L-Highly-Cross-Adsorbed-Secondary-Antibody-Polyclonal/A32754
Donkey anti-Mouse IgG, Alexa Fluor 488	Donkey	Invitrogen, A21202	1:400	https://www.thermofisher.com/antibody/nroduct/Donkey-anti-Mouse-IgG-H-L-Highly-Cross-Adsorbed-Secondary-Antibody-Polyclonal/A-21202

DNA/cDNA Clones

Not applicable

Cultured Cells

Not applicable

Data & Code Availability

Cardiomyocyte computational model files are available for download at the ModelDB portal: (https://senselab.med.yale.edu/modeldb/)

other

Description Source	Repository Persistent ID	URL
Verapamil	Sigma-Aldrich v4629	https://www.sigmaaldrich.com/catalog/product/sigma/v4629
Carbenoxolone	Fisher Scientific 30965–0	https://www.fishersci.com/shop/products/carbenoxolone-disodium-tocris/309650
Di-4-ANEPPS	Invitrogen™ D1199	https://www.fishersci.com/shop/products/di-4-anepps/d1199#
Liberase TM	Sigma-Aldrich 5401127001	https://www.sigmaaldrich.com/catalog/product/roche/libtmro
Sodium Chloride	Sigma-Aldrich S9625	https://www.sigmaaldrich.com/catalog/product/sigald/s9625
Potassium Chloride	Sigma-Aldrich P9541	https://www.sigmaaldrich.com/catalog/product/sigald/p3911
Potassium phosphate monobasic (KH2PO4)	Sigma-Aldrich P0662	https://www.sigmaaldrich.com/catalog/product/sigald/p0662
Sodium phosphate dibasic (Na2HPO4)	Sigma-Aldrich S0876	https://www.sigmaaldrich.com/catalog/product/sial/s0876
Magnesium sulphate heptahydrate (MgSO4.7H2O)	Fisher Scientific M63	https://www.fishersci.com/shop/products/magnesium-sulfate-heptahydrate-crystalline-certified-acs-fisher-chemical-3/M63500
Sodium bicarbonate (NaHCO3)	Sigma-Aldrich S6297	https://www.sigmaaldrich.com/catalog/product/sial/s6297
Potassium bicarbonate (KHCO3)	Sigma-Aldrich P9144	https://www.sigmaaldrich.com/catalog/product/sial/p9144
HEPES buffer solution	Gibco 15630080	https://www.thermofisher.com/order/catalog/product/15630130
Taurine	Sigma-Aldrich T0625	https://www.sigmaaldrich.com/catalog/product/sigma/t0625
Glucose	Sigma-Aldrich G7528	https://www.sigmaaldrich.com/catalog/product/sigma/g7528
2,3-Butanedione monoxime (BDM)	Sigma-Aldrich 31550	https://www.sigmaaldrich.com/catalog/product/sial/31550
Calcium Chloride ($CaCl_2$)	Sigma-Aldrich 499609	https://www.sigmaaldrich.com/catalog/product/aldrich/499609
Donkey Serum	Sigma-Aldrich D9663	https://www.sigmaaldrich.com/catalog/product/sigma/d9663
Fetal Bovine Serum	ThermoFisher A4766801	https://www.thermofisher.com/order/catalog/product/A4766801#/A4766801
Triton X-100	Sigma-Aldrich	https://www.sigmaaldrich.com/catalog/product/sigma/93443
Slides	Fisher Scientific ColorFrost Plus Slides	https://www.fishersci.com/shop/products/fisherbrand-colorfrost-plus-microscope-slides-9/p-4908609
Coverslips	Fisher Scientific	https://www.fishersci.com/shop/products/fisherfinest-premium-cover-glasses-14/p-45380
O.C.T.Compound	Fisher Scientific	https://www.fishersci.com/shop/products/fisher-healthcare-tissue-plus-o-c-t-compound-2/p-4753295
PFA	Sigma-Aldrich P6148	https://www.sigmaaldrich.com/catalog/product/sial/p6148
DAPI	Vectashield, H-1200	http://uat2.vectorlabs.com/vectashield-plus-mounting-medium-with-dapi.html
4-AP	Sigma-Aldrich 275875	https://www.sigmaaldrich.com/catalog/product/aldrich/275875
CsOH	Sigma-Aldrich 232068	https://www.sigmaaldrich.com/catalog/product/aldrich/232068
CsCl	Sigma-Aldrich 203025	https://www.sigmaaldrich.com/catalog/product/aldrich/203025
EGTA	Sigma-Aldrich E3889	https://www.sigmaaldrich.com/catalog/product/sigma/e3889
MgATP	Sigma-Aldrich A9187	https://www.sigmaaldrich.com/catalog/product/sigma/a9187
GTP	Sigma-Aldrich G3776	https://www.sigmaaldrich.com/catalog/product/sigma/g3776
TEA-Cl	Sigma-Aldrich 86614	https://www.sigmaaldrich.com/catalog/product/sigma/86614

Description Source	Repository Persistent ID	URL
TTX	abcam 120055	https://www.abcam.com/tetrodotoxin-citrate-na-channel-blocker-ab120055.html